Title
Ratiometric Sensing of Redox Environments Inside Individual Carboxysomes Trapped in Solution

Journal
The Journal of Physical Chemistry Letters, 13(20)

ISSN
1948-7185

Authors
Carpenter, William B
Lavania, Abhijit A
Borden, Julia S
et al.

Publication Date
2022-05-26

DOI
10.1021/acs.jpclett.2c00782

Peer reviewed

THE JOURNAL OF PHYSICAL CHEMISTRY LETTERS
A JOURNAL OF THE AMERICAN CHEMICAL SOCIETY

pubs.acs.org/JPCL

Letter

Ratiometric Sensing of Redox Environments Inside Individual Carboxysomes Trapped in Solution

William B. Carpenter, Abhijit A. Lavania, Julia S. Borden, Luke M. Oltrogge, Davis Perez, Peter D. Dahlberg, David F. Savage, and W. E. Moerner*

Cite This: J. Phys. Chem. Lett. 2022, 13, 4455−4462

Read Online

ACCESS | Metrics & More | Article Recommendations | Supporting Information

ABSTRACT: Diffusion of biological nanoparticles in solution impedes our ability to continuously monitor individual particles and measure their physical and chemical properties. To overcome this, we previously developed the interferometric scattering anti-Brownian electrokinetic (ISABEL) trap, which uses scattering to localize a particle and applies electrokinetic forces that counteract Brownian motion, thus enabling extended observation. Here we present an improved ISABEL trap that incorporates a near-infrared scatter illumination beam and rapidly interleaves 405 and 488 nm fluorescence excitation reporter beams. With the ISABEL trap, we monitored the internal redox environment of individual carboxysomes labeled with the ratiometric redox reporter roGFP2. Carboxysomes widely vary in scattering contrast (reporting on size) and redox-dependent ratiometric fluorescence. Furthermore, we used redox sensing to explore the chemical kinetics within intact carboxysomes, where bulk measurements may contain unwanted contributions from aggregates or interfering fluorescent proteins. Overall, we demonstrate the ISABEL trap's ability to sensitively monitor nanoscale biological objects, enabling new experiments on these systems.

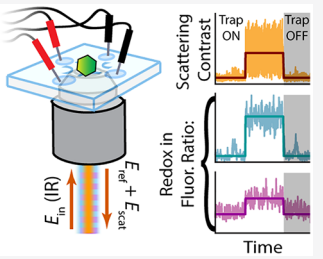

For nanoscale biological objects in solution, Brownian fluctuations dominate their translational dynamics. Because of their stochastic trajectories and fast diffusion, individual objects are commonly immobilized for extended study,[1,2] which may undesirably perturb them from their native states.[1−5] One approach is to use stage motion to rapidly track and follow single particles in solution, which has been demonstrated on particles with diffusion coefficients as large as approximately 10 $\mu m^2/s$.[6−8] To make extended measurements without tethering, anti-Brownian electrokinetic (ABEL) traps have also been developed[9] to apply electrokinetic positional feedback on single fluorescent objects, thereby greatly reducing Brownian motion.[10−12] These traps have been used to directly measure the dynamics of single enzymes,[13] photosynthetic complexes,[14−17] and even single organic fluorophores.[18] Typically, these molecules can be held for seconds, until photobleaching or blinking interrupts continuous positional monitoring.

To overcome the need for fluorescence to estimate position, our lab recently developed the interferometric scattering ABEL (ISABEL) trap, which tracks a nanoparticle's position by its scattering interfered with a local oscillator arising from the back reflection off a water−quartz interface in the sample cell.[19] The interference between the scattered and reflected light enhances the sensitivity by producing a signal that scales linearly with the particle's polarizability, which may be interpreted as mass for objects with fixed composition.[20−22] Our initial study demonstrated trapping of gold nanoparticles as small as 20 nm and showed that polymer nanoparticles down to 50 nm diameter could be held for more than 30 s. Fluorescently labeled particles could also be trapped far beyond the time of photobleaching. Interferometric positional monitoring, independent of fluorescence, opens the door to studying weakly fluorescent biological objects or introducing complex fluorescence excitation protocols.

One such nanoscale biological object is the carboxysome, a proteinaceous microcompartment ∼100 nm in diameter, which is responsible for the fixation of CO_2 into organic carbon in many autotrophic bacteria.[23−26] The chemoautotroph *Halothiobacillus neapolitanus* contains α-carboxysomes, whose operon encodes 10 proteins that collectively assemble into carboxysomes, including rubisco large (CbbL) and small subunits (CbbS), a disordered scaffolding protein (CsoS2), carbonic anhydrase (CsoSCA), two pentameric shell protein paralogues (CsoS4AB), three hexamer shell protein paralogues (CsoS1ABC), and a pseudohexameric shell protein (CsoS1D).[24,27] The self-assembled accumulation of rubisco and carbonic anhydrase inside the roughly icosahedral[28] shell (Figure 1a) has evolved to create a high local concentration of rubisco and CO_2 to overcome rubisco's low turnover rate and outcompete deleterious oxygenation reactions.[29] Functional carboxysomes can also be recombinantly grown in *Escherichia coli*,[23] which aids in inserting fluorescent reporters but also

Received: March 16, 2022
Accepted: May 10, 2022
Published: May 13, 2022

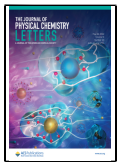

https://doi.org/10.1021/acs.jpclett.2c00782
J. Phys. Chem. Lett. 2022, 13, 4455−4462

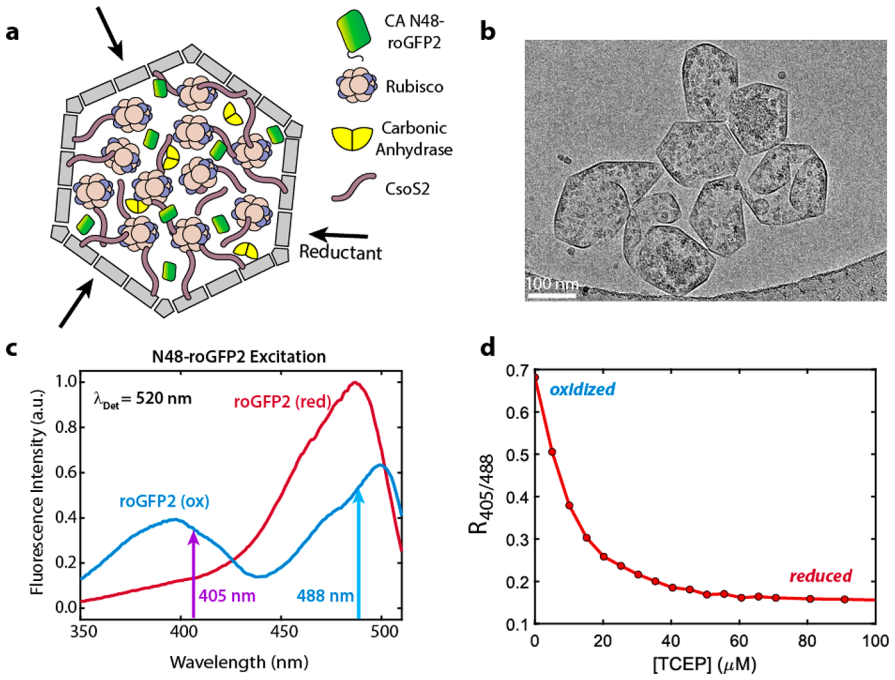

Figure 1. Visualizations of carboxysomes and characteristics of the redox-sensitive GFP mutant roGFP2. (a) The carboxysome consists of a porous proteinaceous shell and the internal cargo rubisco, carbonic anhydrase, and the scaffolding protein CsoS2. roGFP2 is targeted inside the carboxysome using the N-terminal sequence from carbonic anhydrase. (b) Cryo-TEM image of a cluster of α-carboxysomes recombinantly expressed in *E. coli*, demonstrating the variety of shapes, sizes, and integrity. (c) Changes in the fluorescence excitation spectrum of roGFP2 enable ratiometric readout of the redox environment. The fully oxidized spectrum (blue) is bimodal and gives a high fluorescence ratio $R_{405/488}$, while the fully reduced spectrum (red) consists of one peak and produces a low fluorescence ratio. The vertical arrows indicate the excitation wavelengths used in this study for ratiometric measurements. (d) The ratiometric fluorescence from roGFP2 decreases when the reductant TCEP is added.

increases the diversity of shapes, sizes, and integrity of the shell (Figure 1b). This paper reports exclusively on *E. coli*-derived carboxysomes.

Structural and simulation studies posit that the proteinaceous shell preferentially allows the bidirectional diffusion of metabolically important species such as HCO_3^- and ribulose-1,5-bisphosphate[30,31] and therefore is expected to support a chemical environment distinct from the surrounding cytosol.[32,33] The protein shell is also thought to establish a distinctly oxidizing redox environment within the carboxysome relative to the known reducing environment of the cytosol.[29,33−36] However, these hypotheses remain unconfirmed because of the lack of direct measurements on selective shell permeability and redox dynamics. Because of the variation of carboxysome size, shape, and integrity and to mitigate contamination from purification byproducts, it would be highly beneficial to study carboxysomes at the single-particle level. Our goal is not only to trap but also to sense the redox chemical environment inside individual carboxysomes using a local fluorescent protein reporter, roGFP2, which encodes redox information in its fluorescence excitation spectrum (Figure 1c). We have genetically targeted approximately 3−15 copies of roGFP2 inside individual carboxysomes (Figure S1). The ratio of fluorescence brightness from 405 and 488 nm excitation is related to the concentration of reducing species in solution (Figure 1d) and gives a readout that does not rely on the GFP copy number.

To enable fluorescence excitation spectroscopy of roGFP2 inside carboxysomes, we have redesigned the ISABEL trap.[19] In the new configuration (vide infra), the scatter illumination beam has been red-shifted to 800 nm in the near-IR to open up the visible region for fluorescence reporters without photobleaching them. Also, we have introduced two rapidly interleaving excitation beams at 405 and 488 nm to measure the fluorescence emission from roGFP2.[37]

In this work, we directly measured the redox-dependent ratiometric fluorescence of single trapped carboxysomes, where air-oxidized carboxysomes show much more heterogeneous ratiometric fluorescence than reduced carboxysomes. Despite this heterogeneity, we also observed reduction kinetics in carboxysomes after mixing with a reductant, in a first step toward measuring shell permeability. Together, these measurements demonstrate the ability of the ISABEL trap to go beyond synthetic nanoparticles to make extended measurements on single biological objects and show that single-particle measurements on individual carboxysomes provide a new avenue for measuring their physical and chemical properties.

Figure 2 shows the quartz microfluidic trapping cell and the optical layout of the ISABEL trap. Nanoparticles in aqueous solution are allowed to diffuse to the center of the cell's two crossed channels in a region 1.5−2 μm deep (Figure 2a). When an infrared electric field $\mathbf{E}_i$ is incident on the particle, the backscattered field $\mathbf{E}_s$ interferes with the quartz−water interfacial reflection $\mathbf{E}_r$, producing a detected intensity I_{det} given by

$$I_{det} \propto |\mathbf{E}_r + \mathbf{E}_s|^2 = |\mathbf{E}_r|^2 + |\mathbf{E}_s|^2 + 2|\mathbf{E}_r||\mathbf{E}_s| \cos\theta \quad (1)$$

where θ is the phase between the reflected and scattered fields. The last term on the right-hand side of eq 1 represents the interferometric contribution to the intensity, which is linear in the scattered field and thus linear in polarizability and mass for proteinaceous objects.[38] For small particles, $|\mathbf{E}_s|^2$ is negligible, and $|\mathbf{E}_r|^2$ can be obtained by a background measurement when there are no particles in the trapping area. This allows for on-the-

https://doi.org/10.1021/acs.jpclett.2c00782
J. Phys. Chem. Lett. 2022, 13, 4455−4462

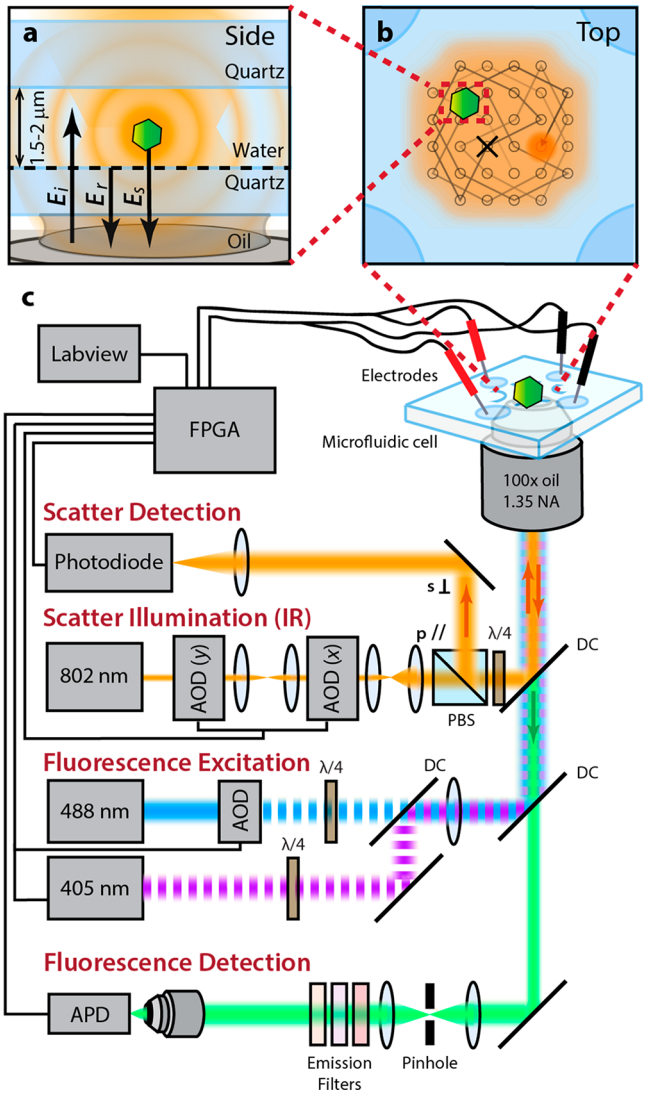

Figure 2. Overview of the ISABEL trap with interleaved fluorescence excitation. (a) A focused incident field E_i illuminates a carboxysome, which radiates the scattered electric field E_s that interferes with E_r, the reflection from the quartz−water interface. (b) Top view of the microfluidic trap, where the incident beam is scanned in a 32-spot Knight's tour pattern. Electrokinetic feedback in two dimensions is applied to the particle to push the object toward a designated location near the center of the illumination scan pattern (marked "×"). (c) Optical paths of the scatter and fluorescence beams, described in more detail in Note S2 and Figure S2. The scatter illumination beam is deflected by two acousto-optic deflectors (AODs) controlled by the field-programmable gate array (FPGA); it is linearly polarized at the polarizing beam splitter (PBS), converted to circular polarization with a quarter-wave plate ($\lambda/4$) to be back-reflected, converted back to the orthogonal linear polarization, and separated for detection on a photodiode. Position is monitored and feedback voltages are calculated on the FPGA and then applied to the solution with platinum electrodes. Simultaneously, the FPGA digitally modulates two CW fluorescence excitation lasers, alternating each millisecond. Fluorescence emission spanning 500−570 nm is collected on an avalanche photodiode (APD) after spatial filtering with a 75 μm pinhole. Detected photons are time-tagged on the FPGA and labeled with the identity of the corresponding excitation laser. AOM, acousto-optic modulator; DC, dichroic beamsplitter.

fly determination of the absolute fractional scattering contrast c as

$$c = \frac{|I_{det} - |\mathbf{E}_r|^2|}{|\mathbf{E}_r|^2} = \frac{2|\mathbf{E}_s||\cos\theta|}{|\mathbf{E}_r|} \quad (2)$$

The particle position is detected by the location of the maximum contrast in the sample plane, obtained from a "Knight's tour" scan pattern of the near-IR beam steered by two acousto-optic deflectors.[10] Rapid positional feedback forces are applied to the solution via voltages calculated on a field-programmable gate array (FPGA) and two pairs of platinum electrodes placed at the ends of the crossed microfluidic channels. The particle is directed to the trap center in two dimensions by electroosmosis.

In addition to the IR trapping beam, the second major difference from previous work is the addition of two visible lasers in wide-field illumination for spectroscopic measurements of the trapped object (Figure 2c). The FPGA digitally modulates each laser power with a 2 ms alternating square wave so that emitted photons from GFP fluorescence can be separated into two excitation channels (Note S2).

Three simultaneous variables are monitored in time for individual trapped carboxysomes: the absolute fractional scattering contrast (Note S3), the emission from 405 nm excitation, and the emission from 488 nm excitation (Figure 3). A step change in the fractional scattering contrast trace at $t \approx 51$ s (Figure 3a, event (i)) shows that when trapping turns on, a diffusing particle becomes trapped for >1 s and then leaves when the feedback is turned off. For these experiments, we toggled feedback on for 2 s and off for 1 s to collect statistics from additional single particles, although we can trap carboxysomes for tens of seconds if desired (Figure S3). The scattering trace of event (i) shows a sudden increase in scattering contrast about a mean value (dark-red line) determined by a changepoint algorithm described below, with wide fluctuations due to the evolving phase θ between $\mathbf{E}_r$ and $\mathbf{E}_s$ as the particle diffuses in the axial direction. Subsequent trapping events display various mean scattering values, indicating a range of particle sizes, including an exceptionally large particle (event (ii)), which is likely an aggregate of multiple carboxysomes and is excluded from further analysis. At $t \approx 75$s (event (iii)), a somewhat small object is trapped, which is then replaced by an object of higher contrast (event (iv)), since anti-Brownian feedback can be applied to only one object at a time.

Simultaneously, we monitor the fluorescence from each carboxysome via the interleaved 405 and 488 nm excitation (Figure 3b,c). Low intensity (<50 W/cm^2) is necessary at 405 nm to balance the roGFP2 emission rate with the light-induced photoconversion[39] of roGFP2 chromophores over extended trapping times (Figures S3 and S4). In event (i), a steady fluorescence level is present in both channels over the trapping time, but particles are brighter and background is lower in the 488 nm channel. Fluorescence changepoints and mean fluorescence brightness were determined with a changepoint-finding algorithm[40] on the 488 nm excitation trace, which provided changepoints to also find the average levels in the scattering and 405 nm traces. Like the various scattering levels, the fluorescence traces show a distribution of brightnesses, indicating variation in roGFP2 loading between carboxysomes. The highly scattering object in event (ii) is accompanied by high brightness in both channels. The object in event (iii) is nonfluorescent, possibly being an emptied carboxysome shell, a protein aggregate that remained after purification, or a dislodged piece of the polyelectrolyte passivation layer (Note S1). Because this particle is nonfluorescent, it is not identified by the

https://doi.org/10.1021/acs.jpclett.2c00782
J. Phys. Chem. Lett. 2022, 13, 4455−4462

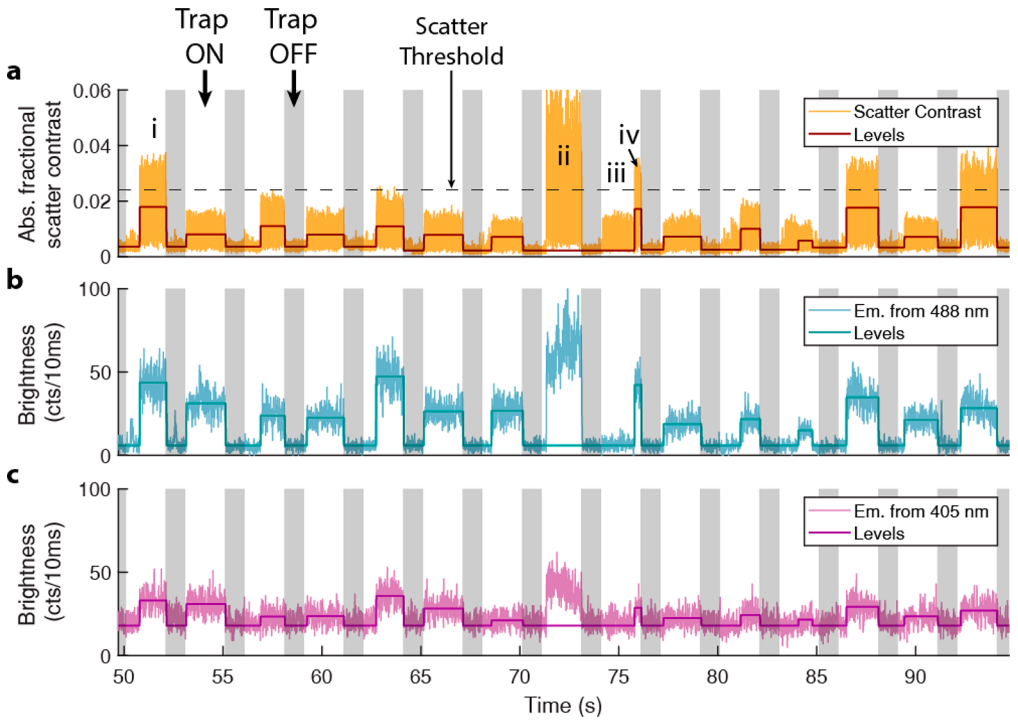

Figure 3. Representative multichannel time traces from a carboxysome trapping experiment in air-oxidized buffer. When positional feedback is turned on (white regions), single detected particles are held at the trap center until feedback is toggled off (gray regions). Trapped roGFP2-labeled carboxysomes display signal in all three channels, such as in event (i). (a) Absolute fractional scatter contrast trace, with individual measurements for each time point (yellow) and average levels for an event (red) determined by the changepoints found on the 488 nm trace (b). The black dashed line indicates the scatter threshold used to reject large aggregates from analysis (Note S3). (b, c) The 488 and 405 nm excitation channels, respectively, and corresponding average levels determined from a changepoint-finding algorithm on the 488 nm trace.

algorithm. Conversely, the object in event (iv) shows signal in all three channels, implying that it is a carboxysome.

The simultaneously measured levels from scattering and fluorescence provide correlated data from individual trapping events, yielding multidimensional statistics measured from carboxysomes in reducing or air-oxidized buffers (Figure 4). Figure 4a–c shows 2D scatter plots from carboxysomes internally reduced by 1 mM TCEP in buffer. In these plots, each point represents the average level found from an individual trapping event, and its color reflects the local density of points.[4] In the Figure 4a marginal histogram, the 488 nm fluorescence distribution is centered at ~60 counts/10 ms but spans 2 orders of magnitude. The 2D scatter plot shows correlation between fluorescence levels and fractional scattering contrast, with subpopulations within the spread. The 2D scatter plot in Figure 4b relating the brightness at 405 nm to scattering shows similar trends, though with lower brightnesses values centered at ~5 counts/10 ms. The scattering constrast histogram (Figure 4c right) appears to be bimodal, peaked at 0.008 and 0.015. In contrast, cryo-TEM imaging reveals that the distribution of carboxysome diameters is unimodal ($\mu \pm \sigma$ = 141 ± 31 nm; Figure S5). Because of the approximate doubling in scattering contrast and unimodal size distribution from cryo-TEM, the higher-contrast peak likely arises from trapped carboxysome dimers. The monomer and dimer populations are not readily separable in a 1D measurement, though they are better separated with our multidimensional correlated measurements.

Turning to redox ratios, Figure 4c shows the 2D scatter plot correlating the reduced roGFP2 fluorescence ratio $R_{405/488}$ with the fractional scattering contrast of each carboxysome. The mean of the ratio distribution is 0.25 (σ = 0.16), a comparatively low value consistent with reducing conditions (Figure S7). To test the ratio uncertainty due to measurement error, we also trapped *E. coli* carboxysomes labeled with superfolder GFP (sfGFP), whose ratiometric fluorescence is not redox-dependent (Figure 4d; also see Figure S8). The tight ratio distribution from sfGFP-labeled carboxysomes indicates that the larger ratio spread in roGFP2 carboxysomes arises from ratio variation between particles. To quantify the measured ratio uncertainty, we propagated the standard errors on the two fluorescence levels into their ratio (Note S4) and present the RMS standard error over all ratios (red error bars in Figure 4c). In sfGFP carboxysomes, the ratio spread is comparable to the RMS uncertainty, indicating that measurement uncertainty dominates the spread. However, for reduced roGFP2 carboxysomes, the ratio distribution exceeds the bounds of the RMS error, indicating other contributions to the ratio spread, which are discussed further below. As well, the ratio distribution for roGFP2 narrows with larger scattering contrast, attributed to increased brightness from higher roGFP2 loading in some carboxysomes. While shot noise dictates that brighter fluorescence increases the absolute noise, the relative noise influencing ratio uncertainty is decreased.

When roGFP2-carboxysomes are left in air-oxidized buffer (Figure 4e–g), they display higher ratios on average (μ = 0.46) and a broader distribution (σ = 0.23). The mean ratio value is consistent with the bulk redox ratio (Figure S7), but the distribution shows an unexpectedly large spread. The RMS standard error of the ratios is comparable to the reduced case but is distinctly smaller than the spread of the oxidized carboxysome ratio distribution, indicating additional heterogeneity. The ratio spread is insensitive to pH, added HCO_3^-, or added oxidant

https://doi.org/10.1021/acs.jpclett.2c00782
J. Phys. Chem. Lett. 2022, 13, 4455−4462

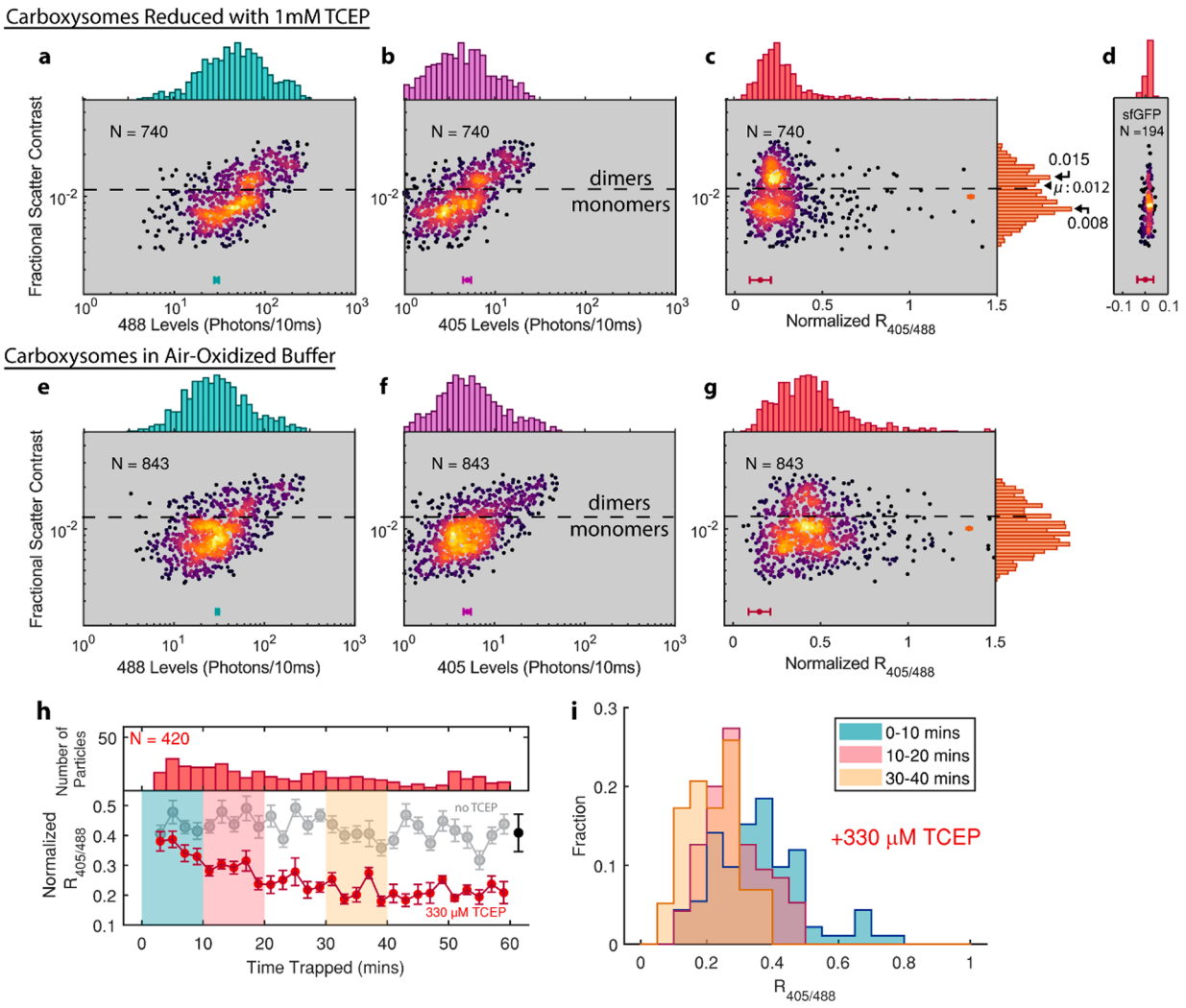

Figure 4. Multidimensional statistics of measurements on individual carboxysomes. (a, b) Scatter plots and marginal histograms between the 488 and 405 nm fluorescence levels, respectively, with fractional scatter contrast, presented on logarithmic axes in both dimensions because of the considerable range measured across carboxysomes. Each point corresponds to a single trapping event, colored by local density of points. The teal and magenta horizontal error bars denote the RMS standard error over all brightness levels. (c) Fractional scattering contrast vs ratiometric fluorescence $R_{405/488}$ for carboxysomes in 1 mM TCEP reducing buffer, with the scattering contrast marginal histogram to the far right. The mean is denoted by μ, and the positions of the two peaks are indicated. Horizontal error bars denote the experimental RMS standard error in ratio uncertainty due to brightness fluctuations about each mean level (Note S4 and Figure S6). (d) Ratio−contrast scatter plot for sfGFP carboxysomes, demonstrating the narrow distribution measured for a reporter independent of redox. (e−g) Fluorescence, scatter contrast, and ratio scatter for carboxysomes in air-oxidized buffer, demonstrating ratios with a higher mean value and wider distribution than reduced carboxysomes. (h) Ratio kinetics measured after mixing with TCEP from individual carboxysomes. Red points correspond to ratios averaged for the number of carboxysomes shown in the top panel in 2 min windows after mixing with 330 μM TCEP, and gray points correspond to carboxysomes without TCEP reductant. Trapping starts approximately 2 min after mixing to load the sample into the cell, thus starting the experiment. Red and gray error bars indicate standard errors of the mean ratio measured in each time bin. The black error bar indicates the same RMS ratio error as in (g). (i) Ratio histograms from the reducing experiment, plotted in 10 min intervals. The distribution is broad and centered at higher values at early times but gradually narrows and shifts to lower values over time.

(1 mM diamide; Figure S8). In particular, roGFP2-labeled carboxysomes are already in fully oxidizing environments when exposed to air. The wide spread of redox ratios likely arises from kinetics of individual roGFP2 molecules, which may occur on multiple time scales: submillisecond time scale protonation/deprotonation kinetics,[41] tens of milliseconds blinking into dark states,[42] and the likely slower kinetics[43] of the binding and unbinding of the engineered disulfide bridge on the roGFP2 β-barrel. The capabilities of the ISABEL trap combined with additional biological constructs will allow further investigation of the heterogeneity in oxidized samples in future work.

Figure 4h,i demonstrates an hour-long reduction kinetics measurement of the ISABEL trap, where fluorescence ratios are measured on individual particles after mixing of air-equilibrated samples into reducing buffer (330 μM TCEP). This measurement can be employed on dilute samples or where it is important to exclude ruptured fragments, large aggregates, and free roGFP2. Here, ratios are collected from individual carboxysomes as in Figure 3 and averaged over 2 min intervals, thus pooling ∼15 carboxysomes for each time point (numbers in upper panel of Figure 4h). After mixing of carboxysomes with reducing buffer, the ratios decrease on a time scale of ∼15 min (red trace in Figure 4h) and settle at the reduced ratio mean of 0.22. This measurement recapitulates the ensemble reduction kinetics (Figure S7), indicating that the bulk measurement is not dominated by external roGFP2. Along with the mean values in

https://doi.org/10.1021/acs.jpclett.2c00782
J. Phys. Chem. Lett. 2022, 13, 4455−4462

each time interval, the single-particle measurements allow us to measure the ratio distribution over time (Figure 4i). In this case, the ratios first show a broader spread ($\sigma = 0.21$ between 0 and 10 min), reflecting both the initially oxidized population and its partial reduction over 10 min. The redox state of the carboxysome population shifts over time to a more equilibrated narrower distribution of reduced carboxysomes ($\sigma = 0.08$ between 30 and 40 min). The capability to select individual particles in a heterogeneous sample and the ability to measure the spread of the redox ratio over time demonstrate the distinct advantages of single-particle over ensemble measurements.

In summary, we have demonstrated that individual carboxysomes can be trapped in solution with active feedback using interferometric detection of their optical scattering from a near-infrared laser. We introduced rapidly interleaving 405 and 488 nm excitation lasers to monitor the ratiometric fluorescence from individual roGFP2-labeled carboxysomes, decoupling the fluorescence channels from the positional monitoring to measure intermittent signals with low excitation intensity. Carboxysomes recombinantly expressed in *E. coli* display wide distributions of scattering contrasts and fluorescence brightness, which can be directly monitored by trapping individual particles. Reduced and oxidized carboxysomes show low and high values of the average redox ratio $R_{405/488}$, respectively. Controlling for chemical environment, single-carboxysome roGFP2 ratios display a wide range of values, indicative of the small numbers ($N \approx 3-15$) of roGFP2 per carboxysome and other sources of heterogeneity, particularly evident in oxidized environments. We can observe minute time scale redox kinetics over the population of carboxysomes, which enables kinetic measurements for biological samples that are highly dilute or contain unwanted contributors to signal such as free roGFP2. Taken together, these experiments demonstrate the ability of the ISABEL trap to monitor nanoscale biological objects like carboxysomes, viruses, and exosomes for extended times and to expand the range of local reporter experiments that can be done in these systems.

■ ASSOCIATED CONTENT

Supporting Information

The Supporting Information is available free of charge at https://pubs.acs.org/doi/10.1021/acs.jpclett.2c00782.

Notes on sample preparation and characterization, ISABEL electronics and optics, analysis and uncertainty estimation, growth and purification of carboxysomes, quantification of roGFP2 brightness and loading, and imaging and sizing of roGFP2-loaded carboxysomes by cryo-EM and supplementary figures showing quantification of roGFP2 loading in carboxysomes, long trapping events, the impact of 405 nm illumination on ratiometric fluorescence, carboxysome sizing with cryo-EM, uncertainty statistics from trapping events, bulk reduction kinetic traces, 2D scatter plots for sfGFP carboxysomes, insensitivity of the ratio distribution with buffer chemistry changes, fluorescence spectra of roGFP2 and dye solution standards, and characterization of the ISABEL PSF (PDF)

Transparent Peer Review report available (PDF)

■ AUTHOR INFORMATION

Corresponding Author

W. E. Moerner − *Department of Chemistry, Stanford University, Stanford, California 94305, United States; Department of Applied Physics, Stanford University, Stanford, California 94305, United States;* orcid.org/0000-0002-2830-209X; Email: wmoerner@stanford.edu

Authors

William B. Carpenter − *Department of Chemistry, Stanford University, Stanford, California 94305, United States;* orcid.org/0000-0002-6174-1035

Abhijit A. Lavania − *Department of Applied Physics, Stanford University, Stanford, California 94305, United States;* orcid.org/0000-0002-8873-0184

Julia S. Borden − *Department of Molecular and Cell Biology, University of California Berkeley, Berkeley, California 94720, United States*

Luke M. Oltrogge − *Department of Molecular and Cell Biology, University of California Berkeley, Berkeley, California 94720, United States;* orcid.org/0000-0001-5716-9980

Davis Perez − *Department of Chemistry, Stanford University, Stanford, California 94305, United States*

Peter D. Dahlberg − *Department of Chemistry, Stanford University, Stanford, California 94305, United States; Division of CryoEM and Bioimaging, SSRL, SLAC National Accelerator Laboratory, Menlo Park, California 94025, United States*

David F. Savage − *Department of Molecular and Cell Biology, University of California Berkeley, Berkeley, California 94720, United States;* orcid.org/0000-0003-0042-2257

Complete contact information is available at: https://pubs.acs.org/10.1021/acs.jpclett.2c00782

Notes

The authors declare no competing financial interest.

The data that support the findings of this study are available from the corresponding author upon request.

■ ACKNOWLEDGMENTS

This work was supported in part by the U.S. Department of Energy, Office of Science, Office of Basic Energy Sciences, Chemical Sciences, Geosciences, and Biosciences Division, Physical Biosciences Program, under Awards DE-FG02-07ER15892 (W.E.M.) and DE-SC0016240 (D.F.S.). P.D.D. was supported in part by the Panofsky Fellowship at the SLAC National Accelerator Laboratory and by Grant 2021-234593 from the Chan Zuckerberg Initiative DAF, an advised fund of Silicon Valley Community Foundation. D.P. was supported by a Stanford Graduate Fellowship.

■ REFERENCES

(1) Okumus, B.; Wilson, T. J.; Lilley, D. M. J.; Ha, T. Vesicle encapsulation studies reveal that single molecule ribozyme heterogeneities are intrinsic. *Biophys. J.* **2004**, *87*, 2798−2806.

(2) Rasnik, I.; McKinney, S. A.; Ha, T. Surfaces and orientations: much to FRET about? *Acc. Chem. Res.* **2005**, *38*, 542−548.

(3) Goldsmith, R. H.; Moerner, W. E. Watching conformational- and photodynamics of single fluorescent proteins in solution. *Nat. Chem.* **2010**, *2*, 179−186.

(4) Squires, A. H.; Dahlberg, P. D.; Liu, H.; Magdaong, N. C. M.; Blankenship, R. E.; Moerner, W. E. Single-molecule trapping and spectroscopy reveals photophysical heterogeneity of phycobilisomes

quenched by Orange Carotenoid Protein. *Nat. Commun.* **2019**, *10*, No. 1172.
(5) Friedel, M.; Baumketner, A.; Shea, J. E. Effects of surface tethering on protein folding mechanisms. *Proc. Natl. Acad. Sci. U.S.A.* **2006**, *103*, 8396−8401.
(6) Cang, H.; Wong, C. M.; Xu, C. S.; Rizvi, A. H.; Yang, H. Confocal three dimensional tracking of a single nanoparticle with concurrent spectroscopic readouts. *Appl. Phys. Lett.* **2006**, *88*, 223901.
(7) McHale, K.; Berglund, A. J.; Mabuchi, H. Quantum dot photon statistics measured by three-dimensional particle tracking. *Nano Lett.* **2007**, *7*, 3535−3539.
(8) Hou, S.; Exell, J.; Welsher, K. Real-time 3D single molecule tracking. *Nat. Commun.* **2020**, *11*, 3607.
(9) Squires, A. H.; Cohen, A. E.; Moerner, W. E. Anti-Brownian Traps. In *Encyclopedia of Biophysics*; Roberts, G. C. K., Watts, A., Eds.; Springer: Berlin, 2018.
(10) Wang, Q.; Moerner, W. Optimal strategy for trapping single fluorescent molecules in solution using the ABEL trap. *Appl. Phys. B: Lasers Opt.* **2010**, *99*, 23−30.
(11) Su, B.; Düser, M. G.; Zarrabi, N.; Heitkamp, T.; Starke, I.; Börsch, M. Observing conformations of single F0F1-ATP synthases in a fast anti-Brownian electrokinetic trap. *Proc. SPIE* **2015**, *9329*, 93290A.
(12) Cohen, A. E.; Moerner, W. E. Suppressing Brownian motion of individual biomolecules in solution. *Proc. Natl. Acad. Sci. U.S.A.* **2006**, *103*, 4362−4365.
(13) Goldsmith, R. H.; Tabares, L. C.; Kostrz, D.; Dennison, C.; Aartsma, T. J.; Canters, G. W.; Moerner, W. E. Redox cycling and kinetic analysis of single molecules of solution-phase nitrite reductase. *Proc. Natl. Acad. Sci. U.S.A.* **2011**, *108*, 17269−17274.
(14) Schlau-Cohen, G.; Yang, H.-Y.; Krueger, T. P. J.; Xu, P.; Gwizdala, M.; van Grondelle, R.; Croce, R.; Moerner, W. E. Single-molecule identification of quenched and unquenched states of LHCII. *J. Phys. Chem. Lett.* **2015**, *6*, 860−867.
(15) Schlau-Cohen, G. S.; Bockenhauer, S.; Wang, Q.; Moerner, W. E. Single-molecule spectroscopy of photosynthetic proteins in solution: exploration of structure−function relationships. *Chem. Sci.* **2014**, *5*, 2933−2939.
(16) Schlau-Cohen, G. S.; Wang, Q.; Southall, J.; Cogdell, R. J.; Moerner, W. E. Single-molecule spectroscopy reveals photosynthetic LH2 complexes switch between emissive states. *Proc. Natl. Acad. Sci. U.S.A.* **2013**, *110*, 10899−10903.
(17) Squires, A. H.; Wang, Q.; Dahlberg, P. D.; Moerner, W. E. A bottom-up perspective on photodynamics and photoprotection in light-harvesting complexes using anti-Brownian trapping. *J. Chem. Phys.* **2022**, *156*, 070901.
(18) Wang, Q.; Moerner, W. E. Lifetime and spectrally resolved characterization of the photodynamics of single fluorophores in solution using the Anti-Brownian Electrokinetic Trap. *J. Phys. Chem. B* **2013**, *117*, 4641−4648.
(19) Squires, A. H.; Lavania, A. A.; Dahlberg, P. D.; Moerner, W. E. Interferometric scattering enables fluorescence-free electrokinetic trapping of single nanoparticles in free solution. *Nano Lett.* **2019**, *19*, 4112−4117.
(20) Gemeinhardt, A.; McDonald, M. P.; König, K.; Aigner, M.; Mackensen, A.; Sandoghdar, V. Label-free imaging of single proteins secreted from living cells via iSCAT microscopy. *J. Vis. Exp.* **2018**, No. e58486.
(21) Lindfors, K.; Kalkbrenner, T.; Stoller, P.; Sandoghdar, V. Detection and spectroscopy of gold nanoparticles using supercontinuum white light confocal microscopy. *Phys. Rev. Lett.* **2004**, *93*, 037401.
(22) Taylor, R. W.; Sandoghdar, V. Interferometric scattering microscopy: seeing single nanoparticles and molecules via Rayleigh scattering. *Nano Lett.* **2019**, *19*, 4827.
(23) Bonacci, W.; Teng, P. K.; Afonso, B.; Niederholtmeyer, H.; Grob, P.; Silver, P. A.; Savage, D. F. Modularity of a carbon-fixing protein organelle. *Proc. Natl. Acad. Sci. U.S.A.* **2012**, *109*, 478.
(24) Oltrogge, L. M.; Chaijarasphong, T.; Chen, A. W.; Bolin, E. R.; Marqusee, S.; Savage, D. F. Multivalent interactions between CsoS2 and Rubisco mediate α-carboxysome formation. *Nat. Struct. Mol. Biol.* **2020**, *27*, 281−287.
(25) Shively, J. M.; Ball, F.; Brown, D. H.; Saunders, R. E. Functional organelles in prokaryotes: polyhedral inclusions (carboxysomes) of *Thiobacillus neapolitanus*. *Science* **1973**, *182*, 584−586.
(26) Heinhorst, S.; Cannon, G. C.; Shively, J. M. Carboxysomes and carboxysome-like inclusions. In *Complex Intracellular Structures in Prokaryotes*; Shively, J. M., Ed.; Springer: Berlin, 2006; pp 141−165.
(27) Yeates, T. O.; Kerfeld, C. A.; Heinhorst, S.; Cannon, G. C.; Shively, J. M. Protein-based organelles in bacteria: carboxysomes and related microcompartments. *Nat. Rev. Microbiol.* **2008**, *6*, 681−691.
(28) Iancu, C. V.; Ding, H. J.; Morris, D. M.; Dias, D. P.; Gonzales, A. D.; Martino, A.; Jensen, G. J. The structure of isolated *Synechococcus* strain WH8102 carboxysomes as revealed by electron cryotomography. *J. Mol. Biol.* **2007**, *372*, 764−773.
(29) Dou, Z.; Heinhorst, S.; Williams, E. B.; Murin, C. D.; Shively, J. M.; Cannon, G. C. CO_2 fixation kinetics of *Halothiobacillus neapolitanus* mutant carboxysomes lacking carbonic anhydrase suggest the shell acts as a diffusional barrier for CO_2. *J. Biol. Chem.* **2008**, *283*, 10377−10384.
(30) Mahinthichaichan, P.; Morris, D. M.; Wang, Y.; Jensen, G. J.; Tajkhorshid, E. Selective permeability of carboxysome shell pores to anionic molecules. *J. Phys. Chem. B* **2018**, *122*, 9110.
(31) Faulkner, M.; Szabo, I.; Weetman, S. L.; Sicard, F.; Huber, R. G.; Bond, P. J.; Rosta, E.; Liu, L.-N. Molecular simulations unravel the molecular principles that mediate selective permeability of carboxysome shell protein. *Sci. Rep.* **2020**, *10*, 17501.
(32) Borden, J. S.; Savage, D. F. New discoveries expand possibilities for carboxysome engineering. *Curr. Opin. Microbiol.* **2021**, *61*, 58−66.
(33) Chen, A. H.; Robinson-Mosher, A.; Savage, D. F.; Silver, P. A.; Polka, J. K. The bacterial carbon-fixing organelle is formed by shell envelopment of preassembled cargo. *PLoS One* **2013**, *8*, No. e76127.
(34) Wang, H.; Yan, X.; Aigner, H.; Bracher, A.; Nguyen, N. D.; Hee, W. Y.; Long, B. M.; Price, G. D.; Hartl, F. U.; Hayer-Hartl, M. Rubisco condensate formation by CcmM in β-carboxysome biogenesis. *Nature* **2019**, *566*, 131−135.
(35) Peña, K. L.; Castel, S. E.; de Araujo, C.; Espie, G. S.; Kimber, M. S. Structural basis of the oxidative activation of the carboxysomal γ-carbonic anhydrase, CcmM. *Proc. Natl. Acad. Sci. U.S.A.* **2010**, *107*, 2455−2460.
(36) Heinhorst, S.; Williams, E. B.; Cai, F.; Murin, C. D.; Shively, J. M.; Cannon, G. C. Characterization of the carboxysomal carbonic anhydrase CsoSCA from *Halothiobacillus neapolitanus*. *J. Bacteriol.* **2006**, *188*, 8087−8094.
(37) Hanson, G. T.; Aggeler, R.; Oglesbee, D.; Cannon, M.; Capaldi, R. A.; Tsien, R. Y.; Remington, S. J. Investigating mitochondrial redox potential with redox-sensitive green fluorescent protein indicators. *J. Biol. Chem.* **2004**, *279*, 13044−13063.
(38) Young, G.; Hundt, N.; Cole, D.; Fineberg, A.; Andrecka, J.; Tyler, A.; Olerinyova, A.; Ansari, A.; Marklund, E. G.; Collier, M. P.; Chandler, S. A.; Tkachenko, O.; Allen, J.; Crispin, M.; Billington, N.; Takagi, Y.; Sellers, J. R.; Eichmann, C.; Selenko, P.; Frey, L.; Riek, R.; Galpin, M. R.; Struwe, W. B.; Benesch, J. L. P.; Kukura, P. Quantitative mass imaging of single biological macromolecules. *Science* **2018**, *360*, 423−427.
(39) Chattoraj, M.; King, B. A.; Bublitz, G. U.; Boxer, S. G. Ultra-fast excited state dynamics in green fluorescent protein: Multiple states and proton transfer. *Proc. Natl. Acad. Sci. U.S.A.* **1996**, *93*, 8362−8367.
(40) Watkins, L. P.; Yang, H. Detection of intensity change points in time-resolved single-molecule measurements. *J. Phys. Chem. B* **2005**, *109*, 617−628.
(41) Oltrogge, L. M.; Wang, Q.; Boxer, S. G. Ground-state proton transfer kinetics in green fluorescent protein. *Biochemistry* **2014**, *53*, 5947−5957.
(42) Schwille, P.; Kummer, S.; Heikal, A. A.; Moerner, W. E.; Webb, W. W. Fluorescence correlation spectroscopy reveals fast optical excitation-driven intermolecular dynamics of yellow fluorescent proteins. *Proc. Natl. Acad. Sci. U.S.A.* **2000**, *97*, 151−156.

https://doi.org/10.1021/acs.jpclett.2c00782
J. Phys. Chem. Lett. 2022, 13, 4455−4462

(43) Cannon, M.; Remington, S. J. Re-engineering redox-sensitive green fluorescent protein for improved response rate. *Protein Sci.* **2006**, *15*, 45−57.

https://doi.org/10.1021/acs.jpclett.2c00782
J. Phys. Chem. Lett. 2022, 13, 4455−4462